Article

Is there a polarization horizon?

Alex S. Hill[1,2,3]*

1   University of British Columbia, Vancouver, BC Canada; ashill@astro.ubc.ca
2   Space Science Institute, Boulder, CO USA
3   Dominion Radio Astrophysical Observatory, National Research Council, Penticton, BC Canada

Abstract: Modern radio spectrometers make measurement of polarized intensity as a function of Faraday depth possible. I investigate the effect of depolarization along a model line of sight. I model sightlines with two components informed by observations: a diffuse interstellar medium with a lognormal electron density distribution and a narrow, denser component simulating a spiral arm or H II region, all with synchrotron-emitting gas mixed in. I then calculate the polarized intensity from $300 - 1800$ MHz and calculate the resulting Faraday depth spectrum. The idealized synthetic observations show far more Faraday complexity than is observed in Global Magneto-Ionic Medium Survey observations. In a model with a very nearby H II region observed at low frequencies, most of the effects of a "depolarization wall" are evident: the H II region depolarizes background emission and less (but not zero) information from beyond the H II region reaches the observer. In other cases, the effects are not so clear, as significant amounts of information reach the observer even through significant depolarization, and it is not clear that low-frequency observations sample largely different volumes of the interstellar medium than high-frequency observations. The observed Faraday depth can be randomized such that it does not always have any correlation with the true Faraday depth.

Keywords: Techniques: radio polarization; ISM: turbulence; ISM: magnetic fields

1. Introduction

Polarized radio continuum emission in the Milky Way typically originates as synchrotron emission caused by relativistic particles accelerating due to magnetic fields. As the polarized emission propagates through the magnetized, ionized component of the interstellar medium (ISM), it undergoes Faraday rotation. A number of physical processes can cause polarization vectors to add destructively, leading to depolarization [1–3]. Uyaniker *et al.* [4] introduced the "polarization horizon", a distance beyond which all emission is depolarized (typically due to a combination of depth and beam depolarization). To first order, the line of sight beyond the polarization horizon does not contribute to the observed polarized emission. The polarization horizon is wavelength, angular resolution, and direction dependent, and true to the metaphor of a horizon is not a solid wall beyond which we cannot see.

With the angular resolution of interferometers, such as the Canadian Galactic Plane Survey (CGPS) observations used by Uyaniker *et al.* [4], depolarization is often evident as a qualitative change in the morphology of the polarized emission. At this meeting, a number of authors presented observations in which there is not clear evidence of a polarization horizon as a general concept. Van Eck *et al.* [5] showed $115 - 178$ MHz LOFAR observations over a $\approx (5°)^2$ field, identifying multiple Faraday depth components and schematically tying them to two nearby primarily-neutral regions within ≈ 300pc. Thomson showed $300 - 480$ MHz data from the all-sky Galactic Magnetoionic Medium Survey (GMIMS) Low Band South (GMIMS-LBS) obtained with the CSIRO Parkes Radiotelescope. In his observations, there is clear depolarization associated with specific H II regions, which I call a "depolarization wall". We also see clear evidence for depolarization in the $1280 - 1750$ MHz GMIMS High Band North (GMIMS-HBN) data, where the W4 superbubble reduces the intensity of Fan Region emission by $\approx 30\%$ [6]. In this case, though depolarization clearly affects the polarized intensity and is associated with ionized gas at a discrete distance in a spiral arm, the depolarization does not appear

to remove all information about the gas behind the depolarizing structure. Because depolarization is purely a polarization effect, there is no corresponding change in the morphology of total intensity images at the same wavelengths. Sun *et al.* [7] used depolarization in GMIMS-HBN data to estimate the distance to the North Polar Spur.

In this contribution, I evaluate the significance of the polarization horizon by integrating increasing distances through a model ISM, assessing the extent to which the polarization horizon metaphor is useful both in terms of the polarized intensity and the measured Faraday depth. To be concrete, I focus my analysis on the GMIMS-HBN and GMIMS-LBS frequency ranges as examples of a relatively high frequency with relatively narrow λ^2 coverage and a relatively low frequency with relatively wide λ^2 coverage, although the analysis is more broadly applicable.

2. Propagation and emission of polarized radiation

Polarized radiation is emitted in the diffuse interstellar medium and propagates to an observer as

$$\mathcal{P} = \int_D^0 \epsilon(s)(\vec{B} \times \hat{s})^2 e^{2i\psi(s,\lambda)} ds. \tag{1}$$

Here $s = 0$ is the observer and $s = D$ is the back of the emission region. The emissivity $\epsilon(s)$ is a function of the relativistic electron density and energy spectrum and the polarization angle at the observer is

$$\psi(s,\lambda) = \psi_0(s) + \phi(s)\lambda^2. \tag{2}$$

Polarized radiation is emitted at the position s with polarization angle ψ_0 and then undergoes Faraday rotation as it propagates from s to the observer proportional to the Faraday depth,

$$\phi(s) = 0.81 \int_s^0 \frac{n_e(s')}{\text{cm}^{-3}} \frac{\vec{B}(s') \cdot \vec{ds'}}{\mu\text{G pc}} \text{ rad m}^{-2}, \tag{3}$$

where n_e is the thermal (non-relativistic) electron density and $\vec{B}$ is the magnetic field. We measure the real and imaginary parts of $\mathcal{P}$ as the Stokes parameters Q and U, respectively. For a slab of uniform density with a uniform magnetic field and uniform synchrotron emissivity ε, equation 1 simplifies to [1]

$$\mathcal{P} = \varepsilon \cdot \left(\frac{\sin \phi\lambda^2}{\phi\lambda^2} \right) e^{2i\psi}, \tag{4}$$

where ϕ and ψ are the Faraday depth and polarization angle integrated through the entire slab.

In the simplest case – that of a background radio source which emits radiation at a uniform angle followed by the radiation propagating through a medium which is uniform in both electron density and magnetic field strength and direction – this propagation results in a simple observed polarization vector in which

$$\psi(\lambda) = \psi_0 + \phi(\text{source})\lambda^2 \equiv \psi_0 + \text{RM}\lambda^2. \tag{5}$$

With observations at as few as two frequencies (though more measurements reduce ambiguities), the rotation measure RM, equivalent to the Faraday depth all the way to the emitting source, and intrinsic polarization angle are easy to derive as the slope and zero-intercept of the observed polarization angle as a function of λ^2.

Burn [1] recognized that with measurements of $\mathcal{P}$ at many frequencies, one can disentangle the signature of multiple components along the line of sight. This is a computationally intensive process which did not become feasible until recently; Brentjens and de Bruyn [8] recognized the power of this technique and coined the term "Faraday tomography." In reality, the ISM is inhomogeneous in n_e, $\vec{B}$, and cosmic ray electron density. The GMIMS survey [9], at 300 MHz $< \nu <$ 1750 MHz, as well as observations with LOFAR and MWA at lower frequencies, exploit the Faraday tomography technique to construct image cubes of diffuse polarized emission as a function of Faraday depth, providing

three-dimensional information about the structure of the magnetized ISM. However, interpretation of these three-dimensional image cubes is complicated by depolarization effects.

In common situations, polarization vectors destructively interfere, causing depolarization. In *bandwidth depolarization*, there is sufficient change in λ^2 within a single channel so that $\Delta\psi = \phi\Delta\lambda^2 \gtrsim 1$ and the channel is depolarized. Here, I consider observations from telescopes with sufficiently narrow channel spacing to avoid bandwidth depolarization. In *geometrical depolarization*, emission components along the line of sight have orthogonal ψ_0. This mechanism is wavelength-independent. I define the models in this paper (§ 3 below) with constant ψ_0, so there is no geometrical depolarization. Note that geometrical depolarization is observed in *Planck* observations at wavelengths where Faraday rotation is negligible [10,11]. *Depth depolarization* is similar to geometrical depolarization but is due to Faraday rotation along the line of sight, causing more distant emission to reach the observer with a polarization orthogonal to closer emission, accounted for by the term in parentheses in equation 4. Depth depolarization is wavelength-dependent and thus can occur in the models presented here. In *beam depolarization*, emission with orthogonal polarization vectors is present within the beam of the telescope, leading to destructive interference. Most commonly, the polarization angle varies within the beam due to individual sightlines with different amounts of Faraday rotation within the beam. This effect depends strongly upon the size of the beam and the observing wavelength. Beam depolarization is often parameterized by the depolarization factor [1],

$$p \equiv \frac{L(\lambda)}{L(0)} = \exp\left(-2\sigma_\phi^2 \lambda^4\right), \tag{6}$$

where σ_ϕ is the standard deviation of the Faraday depths of independent sightlines within the beam, and L is the linearly polarized intensity. This applies when σ_ϕ has a Gaussian distribution. Tribble [12] points out that this approximation only holds when $p \gtrsim 0.5$; at longer wavelengths, the depolarization is less severe,

$$p = \frac{N^{-1/2}}{\sigma_\phi \lambda^2 2\sqrt{2}}, \tag{7}$$

where N is the number of independent sightlines within the beam.

3. Methods

Based on observations of pulsar dispersion and Hα emission, we have reasonable constraints on the electron density distribution in the ISM. The warm ionized medium, which is where most Faraday rotation occurs, is turbulent [13]. Therefore, a series of compressions and rarefactions establishes the electron density structure. This naturally leads to a lognormal distribution of electron density [14,15] which is also inferred from the integrated observables, Hα emission measure EM $= \int n_e^2 \, ds$ and pulsar dispersion measure DM $= \int n_e \, ds$ [16,17].

I have constructed simple numerical models of depolarization of propagating radio waves with inputs listed in Table 1. I begin by assuming a distribution of thermal electron density based on observations of Hα emission and pulsar dispersion. Specifically, I assume a lognormal distribution of n_e and that the ionized gas fills a fraction f of the line of sight. I set $f = 0.5$, consistent with modelling of Hα and pulsar dispersion observations at latitudes $|b| > 10°$ [16], so half of the cells (chosen randomly) have $n_e = 0$ and the densities in the other half are drawn from the lognormal distribution. To this distribution, I add a term modelling a denser region which I refer to as a spiral arm (though it can also be thought of as an H II region depending on the chosen values for n_{arm} and w_{arm}), so

$$n(s) = n_i + n_{\text{arm}} \exp\left(-\frac{(s - d_{\text{arm}})^2}{2w_{\text{arm}}^2}\right) \tag{8}$$

where n_i is drawn from a lognormal distribution with most probable value 10^μ and standard deviation $\sigma_{\log n}$. I construct one model with no arm, one model with an arm 5 kpc from the observer, and one
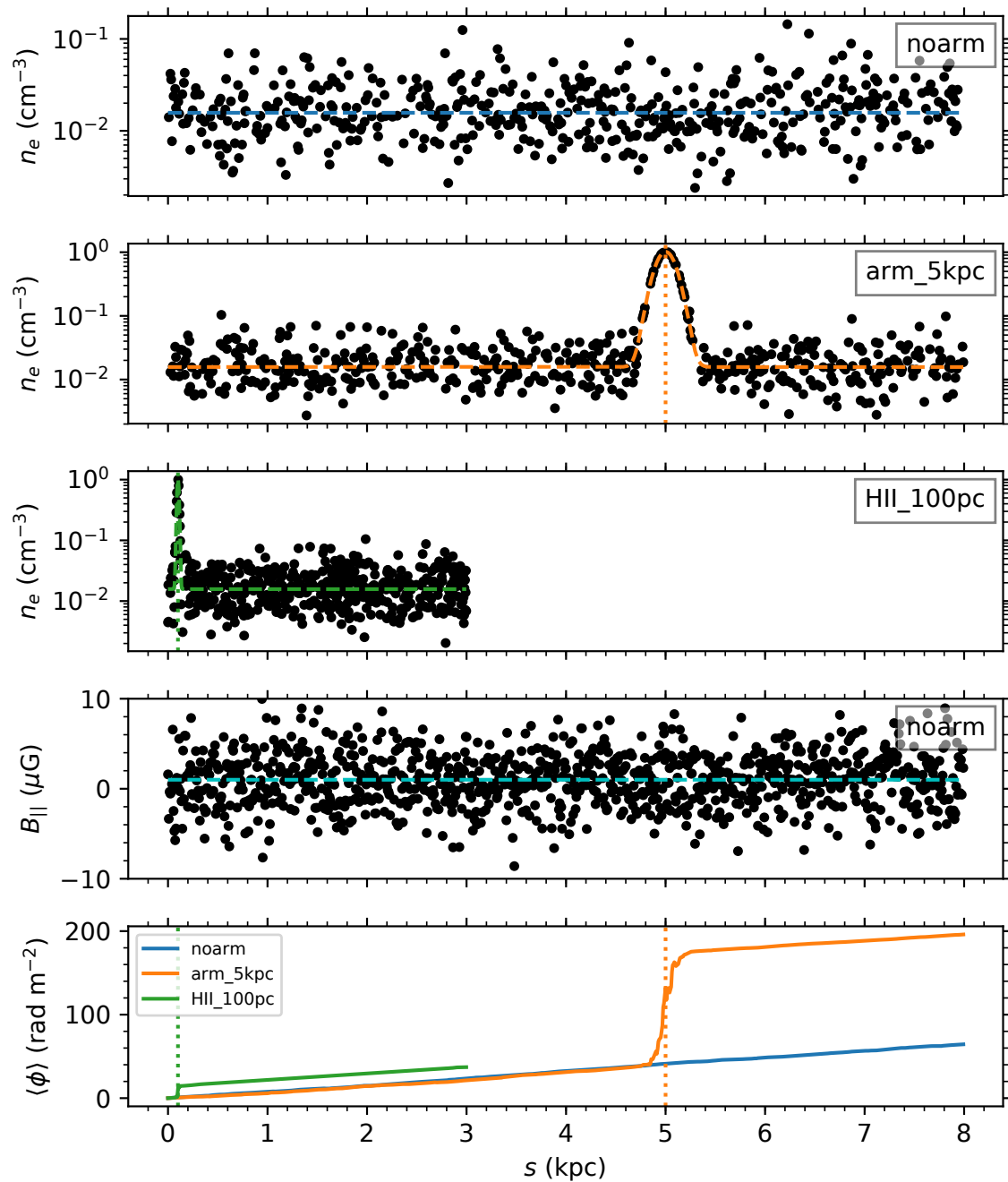
Figure 1. Input density along the line of sight for one sightline in the each model, with parameters listed in Table 1. The "beam" in a given model consists of N sightlines, each chosen from the same distributions as shown here. The fourth panel shows the line-of-sight component of the magnetic field for one model. The bottom panel shows the mean Faraday depth across all the sightlines in each model. Points show the individual cells; dashed lines show the median. Dotted vertical lines show the position of the arm in each model.
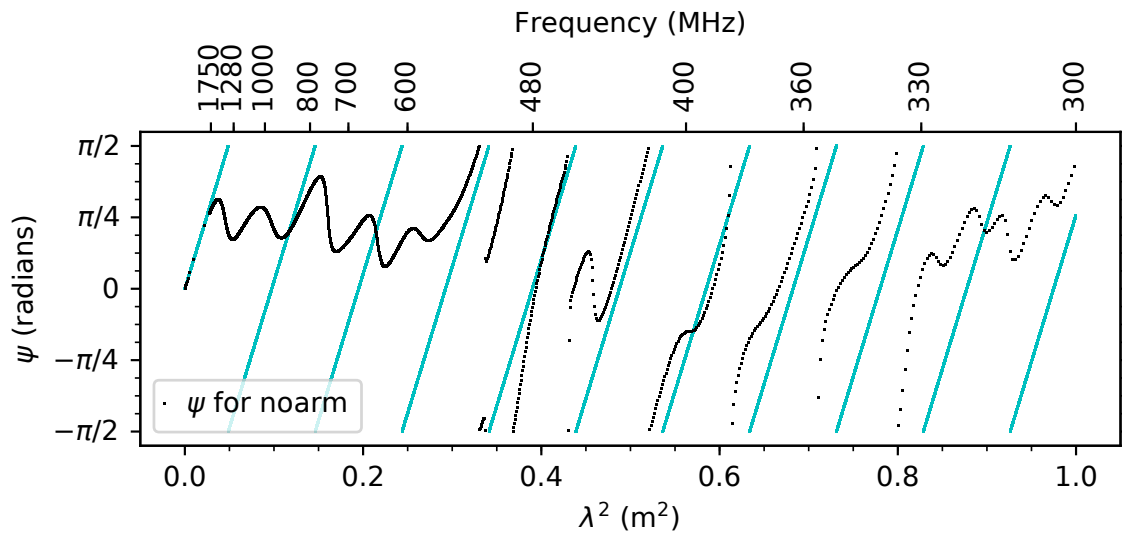
Figure 2. Spectrum of polarization angle as a function of wavelength integrated over a beam (the sum of 25 sightlines) all the way through the `noarm` model, calculated on 0.5 MHz intervals. Cyan lines show the slope $d\psi/d\lambda^2 = \phi/2$, as expected for a Burn [1] slab, where $\phi = 37.1$ rad m^2 is the mean Faraday depth integrated through all sightlines.

model with an "arm" that is very nearby (100 pc) and is more like a nearby, low-density H II region. I also assume a magnetic field geometry loosely informed by models of the Galactic magnetic field [18,19]. The total magnetic field $|\vec{B}|$ is drawn from a Gaussian distribution with mean B_0 and standard deviation σ_B; the line of sight component is $B_{||} = |\vec{B}| \sin\theta$. I further assume a uniform cosmic ray electron density and emissivity $\varepsilon(\lambda = 20\,\mathrm{cm}) = 1$ K/kpc with temperature spectral index $\beta = 3.2$. Figure 1 shows n_e and $B_{||}$ along one sightline as well as the resulting mean Faraday depth ϕ as a function of distance in the three models.

With these inputs, I integrate equations 1 and 3 numerically to calculate the observed polarization vector $\mathcal{P}(\lambda)$ on 0.5 MHz intervals. I run this calculation for independent sightlines and, to simulate the effects of beam depolarization, combine $\mathcal{P}(\lambda)$ from N sightlines. The linearly polarized intensity for the beam is then $L = |\langle\mathcal{P}_i\rangle| = (\langle Q_i\rangle^2 + \langle U_i\rangle^2)^{1/2}$, where the angle brackets denote averaging over the N sightlines, while the polarized intensity for an individual sightline is $L_i = |\mathcal{P}_i|$. I show the spectrum of $\psi = 0.5\arctan(U/Q)$ for one model in Figure 2. From this spectrum, I perform RM synthesis [8] and RM cleaning [20] to calculate the Faraday depth spectrum. I performed RM synthesis in the two GMIMS frequency ranges, but not accounting for radio frequency interferences (RFI) or other excluded frequency channels or any other instrumental limitations. To distinguish the Faraday depth measured from RM synthesis from the true Faraday depth (which is known precisely as a function of s in these models but not in the real ISM), I use the notation $\tilde{\phi}$ to denote the Faraday depth derived from RM synthesis. The input frequency ranges and output maximum value of $\tilde{\phi}$, maximum scale of Faraday depth features, FWHM of the RM transfer function, and the range and chosen resolution $\delta\tilde{\phi}$ of calculated Faraday depth spectra are listed in Table 2, with these values calculated following Schnitzeler *et al.* [21].

By constructing independent sightlines, I neglect projection effects and any correlation between nearby zones at a given distance. Moreover, the assumption that B and n_e are uncorrelated is unlikely to be true in reality. The Faraday depth in this model is the integral of the product of a Gaussian (B) and a lognormal (n_e) distribution and therefore is itself neither Gaussian nor lognormal. Therefore, the assumption of a Gaussian distribution in the derivation of equations 6 and 7 does not apply. I also treat all sightlines as in the plane of the Galaxy, neglecting the different vertical distributions of the

Table 1. Input parameters

Name	10^μ (cm^{-3})	$\sigma_{\log n}$	f	n_{arm} (cm^{-3})	d_{arm} (pc)	w_{arm} (pc)	DM (pc cm^{-3})	B_0 (μG)	σ_B (μG)	θ	N
`noarm`	0.016	0.30	0.5	0.0	...	...	78.6	1.0	3.0	45°	25
`arm_5kpc`	0.016	0.30	0.5	1.0	5000	100	204.8	1.0	3.0	45°	25
`HII_100pc`	0.016	0.30	0.5	1.0	100	10	42.2	1.0	3.0	45°	25

Table 2. RM synthesis parameters

Survey	Frequencies (MHz)	$\delta\nu$	$\tilde{\phi}_{\max}$	Max scale	FWHM	Range	$\delta\tilde{\phi}$
					(rad m^{-2})		
GMIMS-LBS	$300-480$	0.5	570	8.0	6.2	$-300 < \tilde{\phi} < +300$	1
GMIMS-HBN	$1280-1750$	0.5	44 000	107	149	$-600 < \tilde{\phi} < +600$	5

thermal electrons, relativistic electrons, and magnetic fields as well as reversals or other changes in the mean magnetic field along the sightline; Sokoloff *et al.* [2] address these cases. Because this model assumes sightlines in the midplane but the $f = 0.5$ assumption is based on modelling of sightlines which sample the entire WIM disk, the filling fraction may be overestimated. The effect of this would simply be for the numerical values of the distances in this paper to be lower than the distances they model in the real Galaxy.

4. Results

The spectrum in Figure 2 shows the impact of Faraday rotation and depolarization effects. First, the different λ^2 coverages of the GMIMS-LBS ($300 - 480$ MHz) and GMIMS-HBN ($1280 - 1750$ MHz) surveys are evident from the top axis. In the GMIMS-LBS band, the polarization angle rotates many times through π radians. At frequencies $\nu \gtrsim 500$ MHz, there are no more π radian rotations in the polarization angle. Instead, ψ oscillates on a period of ≈ 0.05 m^2. There is always a limit in which a spectral window is narrow enough so that the data are consistent with a straight line (even if it is sampled at a sufficient number of frequencies to avoid the $n\pi$ ambiguity); in such a narrow window, a single rotation measure would describe the data fully. We therefore must consider whether our λ^2 coverage is sufficient to be comfortably out of that limit; this is one definition of "wide" λ^2 coverage. Most windows with the λ^2 coverage of the GMIMS-HBN data are narrow enough to be in this situation. Moreover, both the magnitude and the sign of the derived rotation measure in these windows — especially at $\nu \gtrsim 600$ MHz in the example in Figure 2 — can change depending on the chosen spectral window: these windows may contain insufficient variation in ψ for the RM synthesis process to identify even the correct sign of ϕ. Therefore, *it is plausible and even likely that the sign of the Faraday depth derived from emission over a narrow λ^2 range in a given observation will disagree with the sign of the rotation measure towards a background point source.* In this situation, $\tilde{\phi}$ could have a negative sign even though there is no volume along the sightline in which ϕ is negative. The highest frequency at which π radian rotations occur is ≈ 650 MHz in the `arm_5kpc` model, and in the `HII_100pc` model, there are π radian rotations down to $\lambda^2 = 0$, so this behavior is dependent upon the depolarizing structures in the ISM.

From equation 6, we expect beam depolarization to cause the polarization horizon to be approached when $\sigma_\phi^2 \lambda^4 \gtrsim 1$. This is shown in Figure 3 at two wavelengths, $\lambda = 70$ cm (in the GMIMS-LBS band) and $\lambda = 20$ cm (in the GMIMS-HBN band). At 20 cm, this threshold is never reached in the `noarm` model but is reached in the spiral arm at $s = 5$ kpc in model `arm_5kpc` and (marginally) in the H II region at $s = 100$ pc in model `HII_100pc`. At $\lambda = 70$ cm, this threshold is reached in the H II region in that model and by $s \approx 1$ kpc in the other two models. Therefore, we expect the polarization horizon in the long-wavelength case to be quite nearby. At the other extreme,
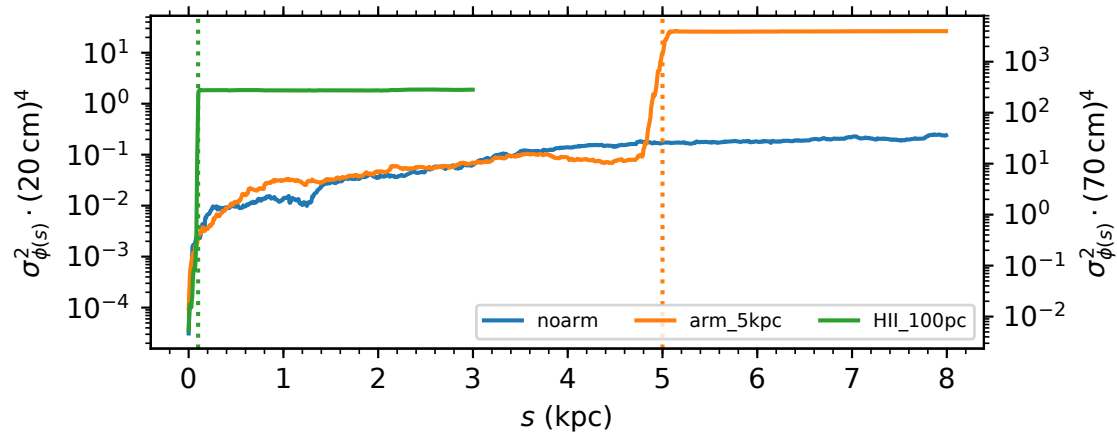
Figure 3. The factor in equation 6, $\sigma_\phi^2 \lambda^4$ for each of the models. The left axis values are labeled for $\lambda = 20\,\text{cm}$; the right axis values are labeled for $\lambda = 70\,\text{cm}$. When $\sigma_\phi^2 \lambda^4 \gg 10^0$, total depolarization is expected. Dotted vertical lines show the position of the arm in each model.

beam depolarization is not likely to cause a polarization horizon at the shorter wavelength at all in the `noarm` model, although other depolarization effects could.

I show the output polarized intensity and polarization angle as a function of D at the same two single wavelengths in each of the three models in Figure 4. The dashed lines show the polarized intensity of an individual sightline, which cannot include any beam depolarization effects. At $\lambda = 70\,\text{cm}$ (Fig. 4a), the polarized intensity increases and decreases with distance due to the oscillatory effects of depth depolarization (Equation 4). The solid lines show the entire beam, which does include beam depolarization effects in addition to depth depolarization. In all cases, in the absence of any depolarization, the polarized intensity would be

$$L = \int_D^0 \varepsilon(s)ds = \varepsilon\,D\left(\frac{\lambda}{20\,\text{cm}}\right)^\beta \tag{9}$$

for the inputs chosen in the model; this is shown with the black dot-dashed line. The polarized intensity in individual sightlines oscillates with distance and, after a distance such that $\phi(D)\lambda^2 \gtrsim 1$, is much lower than that in equation 9 due to depth depolarization. However, because n_e and $B_{||}$ are drawn from non-uniform distributions, depth depolarization never produces the complete nulls implied by equation 4.

In Figure 5, I show the polarized intensity from the `noarm` model compared to the predicted effects of depth and beam depolarization. At $\lambda = 20\,\text{cm}$ (bottom panel), the polarized intensity measured for the beam decreases from 100% of the mean polarized intensity of the individual sightlines at $s = 0$ to $\approx 75\%$ of that of the individual sightlines at $s = 8\,\text{kpc}$. The depth depolarization model (brown dotted line) accurately describes the mean of the individual sightlines (red dashed line); beam depolarization without considering depth depolarization (purple dotted line) does not. At this wavelength, the first depth depolarization null is not reached in 8kpc. The combination of depth and beam depolarization (pink dotted line) produces a polarized intensity somewhat lower than predicted by equation 6. This is unsurprising because of the assumed Gaussian distribution of ϕ, which we does not describe our model.

At $\lambda = 70\,\text{cm}$, the first depth depolarization null is reached after $\approx 700\,\text{pc}$ (brown dotted line in Figure 5, top panel), calculated using $\phi\lambda^2 = \pi$ from equation 4 with the mean value of ϕ across all sightlines. In a representative individual sightline (green dashed line), the polarized intensity comes close to zero but never fully reaches zero because n_e and $B_{||}$ are not uniform. The mean polarized
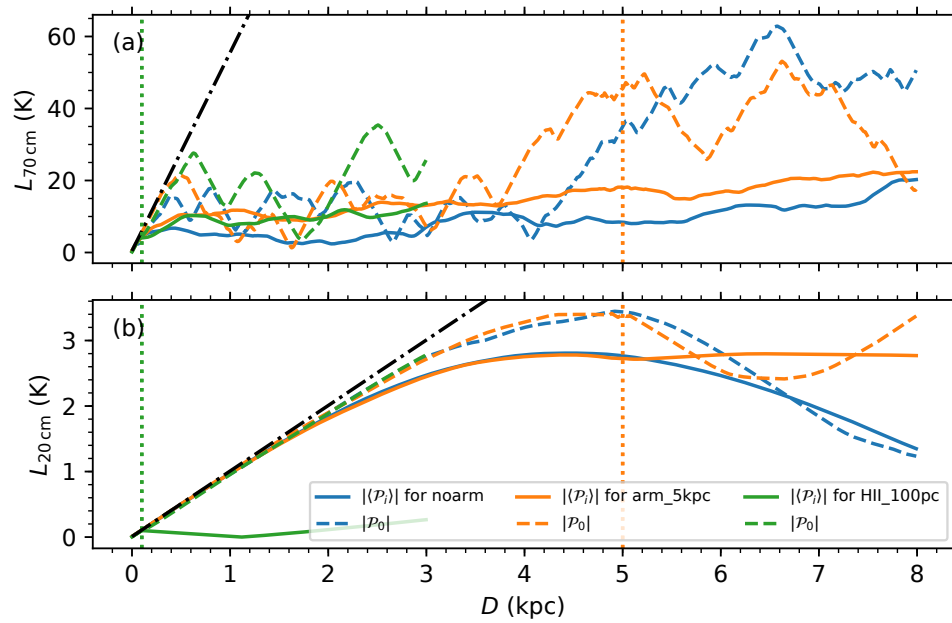
Figure 4. Polarized intensity as a function of D, the integration limit in equation 1, at $\lambda = 70\,\text{cm}$ (top) and $20\,\text{cm}$ (bottom). The solid lines show the polarized intensity over the beam, $|\langle \mathcal{P}_i \rangle|$. The dashed lines show the polarized intensity in one randomly chosen individual sightlines within the beam, $|\mathcal{P}_i|$. Vertical dotted lines show the position of the spiral arm in the model with the corresponding color. Dot-dashed lines show the polarized intensity in the absence of depolarization effects (equation 9). Note that integrated polarized intensites (moment 0) are shown in Figure 7 below. Dotted vertical lines show the position of the arm in each model.
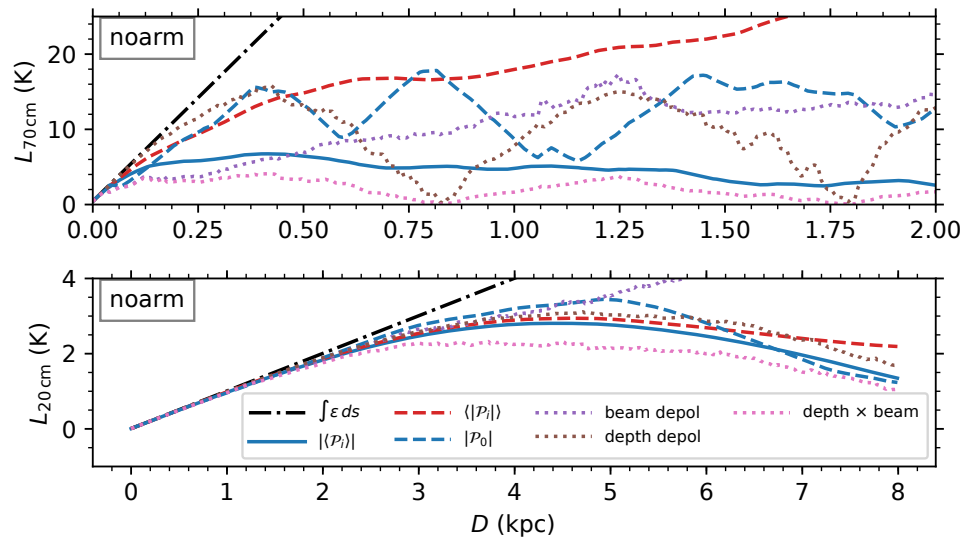

Figure 5. Blue lines are as in Figure 4: polarized intensity for the full beam (blue solid line) and in a representative sightline within the beam (blue dashed line) from the `noarm` model as a function of D. I also show the mean of $|\mathcal{P}_i|$, $\langle |\mathcal{P}_i| \rangle$, of the $N = 25$ individual sightlines (red dashed line). Dotted lines show analytic models of beam depolarization (equations 6 and 7), depth depolarization (equation 4), and both. Note that in the top ($70\,\text{cm}$) panel, I show only the first 2 kpc because depolarization effects become dominant on shorter distance scales at the long wavelength.
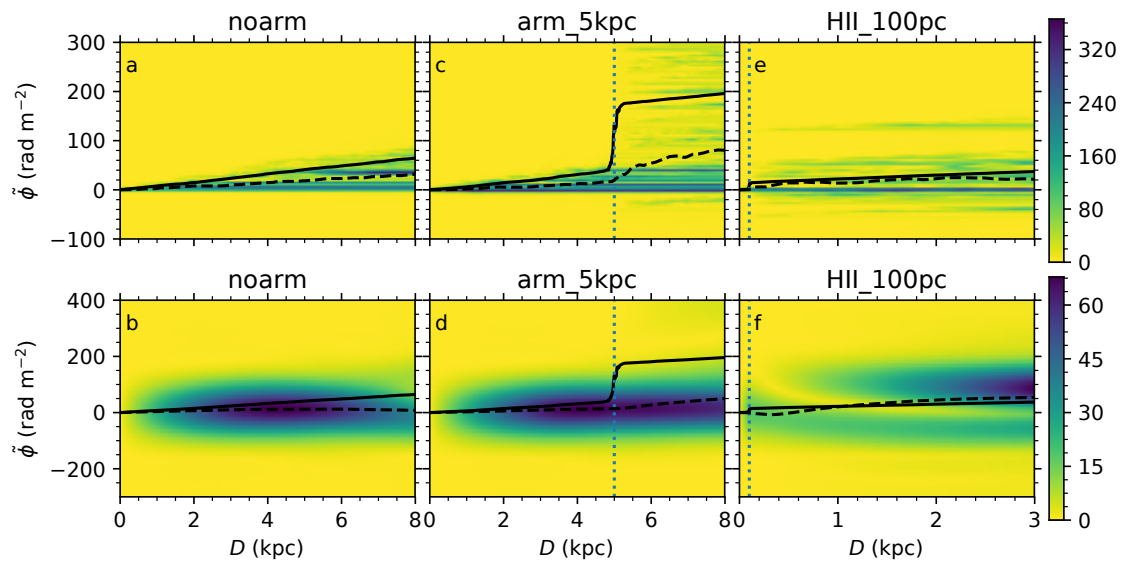
Figure 6. Faraday depth spectrum as a function of D as measured in the GMIMS-LBS frequency band (top) and the GMIMS-HBN frequency band (bottom). The simulated polarized intensity in K is indicated with the color bars. Solid lines show ϕ integrated to $s = D$; dashed lines show the first moment of the Faraday depth spectra. Dotted vertical lines show the position of the arm in each model.

intensity across all sightlines (orange dashed line) never approaches zero because the locations of the nulls are out of phase in the different sightlines. The polarized intensity measured for the beam (blue solid line) is much smaller than the mean polarized intensity for the individual sightlines, indicating strong beam depolarization. However, equations 6 and 7 again overestimate the effects of beam depolarization; the polarized intensity across the beam is a factor of > 2 larger than predicted (purple dotted line) for most values of D.

In Figure 6, I show the effect of depolarization on the polarized intensity measured using RM synthesis. In the `noarm` model, as one integrates further along the line of sight to emission regions at higher Faraday depths, the Faraday spectrum has power at Faraday depths ranging from zero to $\phi(D)$, most clearly in the LBS band (Figure 6a). In the `arm_5kpc` model, the effects of the arm are evident in Figure 6c,d in both frequency ranges: the arm shifts some of the emission to much higher $\tilde{\phi}$, including Faraday depths much higher than the mean $\phi(5\,\text{kpc})$. However, there is little impact on the *total* polarized intensity either at a single frequency (Figure 4) or in the Faraday depth spectra (Figure 6) or moment 0 (Figure 7).

Figure 7 shows moments of Faraday depth [22], analogous to moments of spectral lines. Moment 0 shows the polarized intensity integrated across all Faraday depths, moment 1 shows the polarized intensity-weighted mean Faraday depth, and moment 2 shows the intensity-weighted width of the Faraday depth spectra. From the moment 0 panel, it is clear that the LBS polarized intensity (dashed lines) increases approximately monotonically with distance in all models, even beyond the depolarizing features.

5. Discussion: Is there a polarization horizon?

In the models presented here, depolarization acts on the single-frequency polarized intensity largely in accordance with the models by Burn [1], Tribble [12], and Sokoloff *et al.* [2]. The behavior is qualitatively different at $\lambda = 70\,\text{cm}$ than at 20 cm: at the longer wavelength, beam depolarization effects due to the diffuse ISM dominate within a few hundred pc, before depth depolarization effects
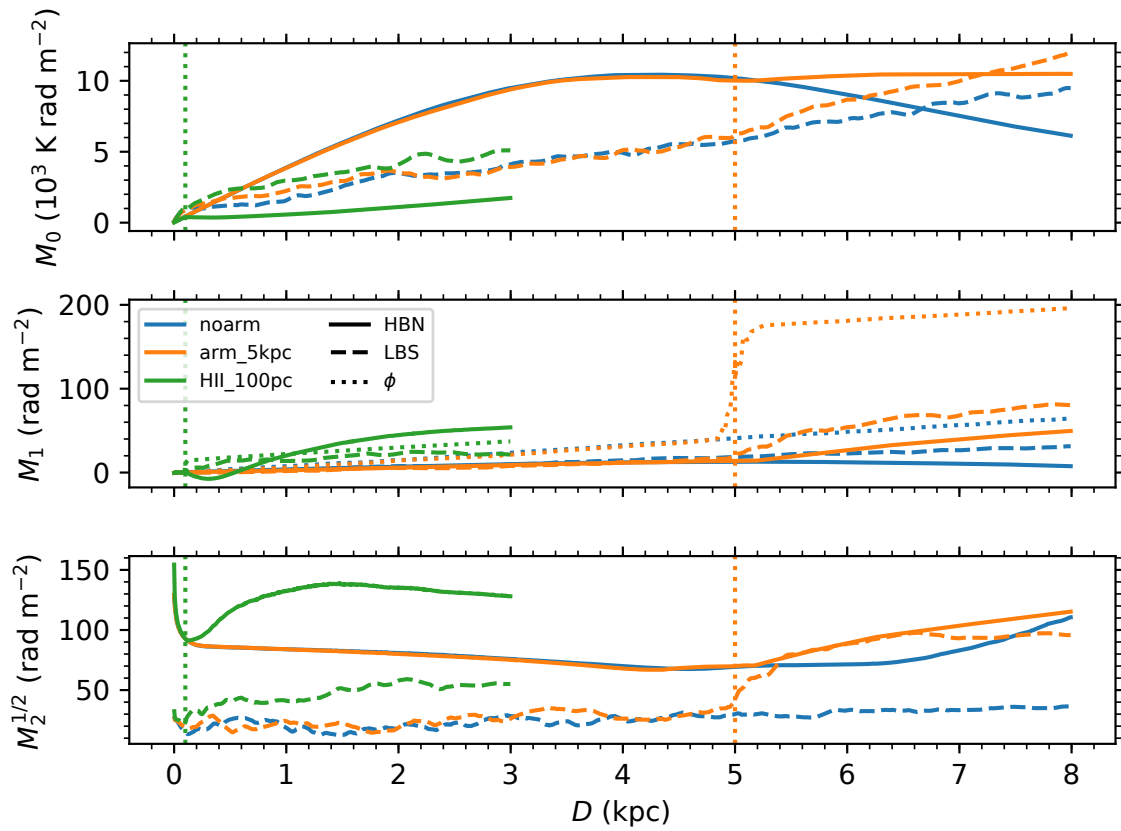
Figure 7. Moments of the Faraday depth spectrum as a function of distance along the sightline. Solid lines show the GMIMS-HBN Faraday spectrum; dashed lines show the GMIMS-LBS Faraday spectrum. The zeroth moment is the polarized intensity integrated across the Faraday spectrum, $M_0 = \int L \, d\phi$. The first moment is the intensity-weighted Faraday depth, $M_1 = \int L\phi \, d\phi / M_0$; the dotted lines show the true ϕ for the input model (from Figure 1), which is in principle the rotation measure one would measure towards a point source at distance D (or a background point source for the maximum value of D). The second moment is the intensity-weighted width of the Faraday depth spectrum, $\int L \cdot (\phi - M_1)^2 d\phi / M_0$; $M_2^{1/2}$ is shown. Dotted vertical lines show the position of the arm in each model.

become important, while at 20 cm, depth depolarization is more important than beam depolarization with 25 sightlines within the beam.

There is a distance beyond which depolarization effects become evident. Especially in model `HII_100pc` observed at long wavelengths, that distance is very short, as predicted by the Burn [1] model: $\sigma_\phi^2 \lambda^4 \gtrsim 1$ at $s \gtrsim 90$ pc. In that most extreme case, integrating further beyond the depolarizing structure leads to relatively little change in the polarized intensity at 70 cm. However, although the polarized intensity at the single frequency shown no longer increases with distance, the Faraday spectrum (Figure 6e) and the moments (green dashed lines in Figure 7) do continue to evolve. This is the closest case in these models to the "depolarization wall", but the wall is not opaque to polarized radiation. Similarly, in the other models and in both frequency ranges, there is no physical distance beyond which further integration does not affect at least some aspects of the observed spectrum. Therefore, though it is probably reasonable to say that there is a different (but difficult to precisely define) weighting function to the volume sampled by polarization observations at different frequencies (with longer-wavelength observations weighted more towards a more nearby volume, especially in the

`HII_100pc` model), these models suggest that longer wavelengths do not sample an entirely different volume than the shorter wavelengths.

In the same model observed at longer wavelengths, again the polarized intensity changes, first decreasing until $D \approx 1.1\,\mathrm{kpc}$ and then increasing, presumably due to depth depolarization effects (green line in Figure 4b). However, the Faraday depth spectrum changes considerably as we integrate further (Figure 6f). In fact, the Faraday depth spectrum bifurcates into two components, with one at $\tilde{\phi} \approx -60\,\mathrm{rad\,m^{-2}}$ and one at $\tilde{\phi} \approx +90\,\mathrm{rad\,m^{-2}}$ even though there is no emission component at *either* Faraday depth; all of the gas in the model is found at $0 \lesssim \phi \lesssim +40\,\mathrm{rad\,m^{-2}}$.

The situation is rather less hopeless for the first Faraday moments shown in Figure 7 and as dashed lines in Figure 6 than for the individual components. Indeed, the first moments of $\tilde{\phi}$ are generally close to $\phi/2$ for the models in which the emission and rotation are mixed, as expected for a Burn slab. Moreover, in the `HII_100pc` model (Figure 6e,f), the first moment of $\tilde{\phi}$ is approximately ϕ. This is expected because most of the Faraday rotation occurs in the H II region at $s = 100\mathrm{pc}$, so most of the emission occurs behind most of the Faraday rotation. However, evidently the H II region again does not fully block information about the ISM beyond it, even though $\sigma_\phi^2 \lambda^4 \sim 10^{2.5}$ at $\lambda = 70\,\mathrm{cm}$ (Figure 3): the measured first moment increases from $\tilde{\phi}(200\,\mathrm{pc}) = +5.9\,\mathrm{rad\,m^{-2}}$ to $\tilde{\phi}(1\,\mathrm{kpc}) = +13.5\,\mathrm{rad\,m^{-2}}$ to $\tilde{\phi}(3\,\mathrm{kpc}) = +21.4\,\mathrm{rad\,m^{-2}}$. With the moments, we lose the complexity in the Faraday spectrum. However, RM synthesis with moments still benefits from the wide λ^2 coverage, averaging over the $\sin(\phi\lambda^2)/\phi\lambda^2$ behavior of depth depolarization.

Different observed Faraday depths at different wavelengths are often interpreted as evidence that the different wavelength observations are sampling different volumes of the ISM because of the moving polarization horizon. However, this picture does not describe the model presented here. In particular, as discussed at the beginning of Section 4, the sign of the rotation measure can change depending on the portion of the frequency spectrum (Figure 2) being sampled in the `noarm` model. There is no portion of any of the models presented here with a negative ϕ, yet $\tilde{\phi}$ can have components with a negative centroid both at HBN and LBS frequencies (Figure 6). Therefore, depolarization effects lead not to a Faraday spectrum that samples a different volume but measured values of $\tilde{\phi}$ that do not map to ϕ in an obvious way.

In conclusion, I find that both discrete depolarizing structures and an extended medium with non-uniform electron density and magnetic field can create a distance at which the polarization effects begin a sunset. However, integrating further through the medium does continue to lead to changes in the observables: information reaches us from beyond the polarization horizon.

In this work, I describe the Faraday spectra from individual realizations of a beam. Given the parameters I chose, the details vary significantly in different realizations. A detailed description of the possible spectra for a given set of parameters is beyond the scope of this work, as is an exploration of the many free parameters such as the chosen position of the spiral arms, the density distribution, and variations with Galactocentric radius, Galactic longitude, and latitude. Instead, I attempt to give a qualitative understanding of the implications of this model from calculations performed on a laptop. I have tested many different realizations of the model, and the general findings hold. I have also tried different parameter choices; the three models I chose to present are representative examples of three different cases which highlight distinct effects in the GMIMS-HBN and GMIMS-LBS frequency ranges.

It is also not clear that the synthetic Faraday spectra presented here look anything like any observed Faraday spectra; they do not look like the Faraday spectra seen in GMIMS observations, which even in GMIMS-LBS data do not typically show the many components evident in Figure 6a,c,e (M. Wolleben et al. in prep). However, LOFAR Faraday depth spectra presented by Van Eck *et al.* [5, and at this meeting] do show notably complex spectra. Due primarily to RFI, the spectral sampling in GMIMS data is intermittent, which will likely map to incomplete sampling of Faraday depth space. These models provide insight into the behavior of polarized radiation in the ISM. However, these impacts are far easier to see in a semi-analytic model such as the one presented here; it is not immediately obvious how to map this information onto real observations. Testing these models with

observations will require generating many realizations of the models to generate statistics and synthetic images as seen only at the observer, beyond the scope of this work. In particular, one could use an extended region derived from many realizations of the `noarm` model as a background and add a region with a radius of several beams from the `HII_100pc` model to see if the resulting image is qualitatively similar to observed depolarizing screens [4,23, and Thomson's work at this meeting].

1. Burn, B.J. On the depolarization of discrete radio sources by Faraday dispersion. *MNRAS* **1966**, *133*, 67.
2. Sokoloff, D.D.; Bykov, A.A.; Shukurov, A.; Berkhuijsen, E.M.; Beck, R.; Poezd, A.D. Depolarization and Faraday effects in galaxies. *MNRAS* **1998**, *299*, 189–206.
3. Gaensler, B.M.; Dickey, J.M.; McClure-Griffiths, N.M.; Green, A.J.; Wieringa, M.H.; Haynes, R.F. Radio Polarization from the Inner Galaxy at Arcminute Resolution. *ApJ* **2001**, *549*, 959–978.
4. Uyaniker, B.; Landecker, T.L.; Gray, A.D.; Kothes, R. Radio Polarization from the Galactic Plane in Cygnus. *ApJ* **2003**, *585*, 785–800.
5. Van Eck, C.L.; Haverkorn, M.; Alves, M.I.R.; Beck, R.; de Bruyn, A.G.; Enßlin, T.; Farnes, J.S.; Ferrière, K.; Heald, G.H.; Horellou, C.; Horneffer, A.; Iacobelli, M.; Jelic, V.; Martí-Vidal, I.; Mulcahy, D.D.; Reich, W.; Röttgering, H.J.A.; Scaife, A.M.M.; Schnitzeler, D.H.F.M.; Sobey, C.; Sridhar, S.S. Faraday tomography of the local interstellar medium with LOFAR: Galactic foregrounds towards IC 342. *A&A* **2017**, *597*, A98.
6. Hill, A.S.; Landecker, T.L.; Carretti, E.; Douglas, K.; Sun, X.H.; Gaensler, B.M.; Mao, S.A.; McClure-Griffiths, N.M.; Reich, W.; Wolleben, M.; Dickey, J.M.; Gray, A.D.; Haverkorn, M.; Leahy, J.P.; Schnitzeler, D.H.F.M. The Fan Region at 1.5 GHz - I. Polarized synchrotron emission extending beyond the Perseus Arm. *MNRAS* **2017**, *467*, 4631–4646.
7. Sun, X.H.; Landecker, T.L.; Gaensler, B.M.; Carretti, E.; Reich, W.; Leahy, J.P.; McClure- Griffiths, N.M.; Crocker, R.M.; Wolleben, M.; Haverkorn, M.; Douglas, K.A.; Gray, A.D. Faraday Tomography of the North Polar Spur: Constraints on the Distance to the Spur and on the Magnetic Field of the Galaxy. *ApJ* **2015**, *811*, 40.
8. Brentjens, M.A.; de Bruyn, A.G. Faraday rotation measure synthesis. *A&A* **2005**, *441*, 1217–1228.
9. Wolleben, M.; Landecker, T.L.; Carretti, E.; Dickey, J.M.; Fletcher, A.; Gaensler, B.M.; Han, J.L.; Haverkorn, M.; Leahy, J.P.; McClure-Griffiths, N.M.; McConnell, D.; Reich, W.; Taylor, A.R. GMIMS: the Global Magneto-Ionic Medium Survey. Cosmic Magnetic Fields: From Planets; Strassmeier, K.G.; Kosovichev, A.G.; Beckman, J.E., Eds. NRC Herzberg Institute of Astrophysics, DRAO, Penticton, BC, V2A6J9, Canada; Covington Fellow, Cambridge University Press, 2009, pp. 89–90.
10. Miville-Deschênes, M.A.; Ysard, N.; Lavabre, A.; Ponthieu, N.; Macías-Pérez, J.F.; Aumont, J.; Bernard, J.P. Separation of anomalous and synchrotron emissions using WMAP polarization data. *A&A* **2008**, *490*, 1093–1102.
11. Delabrouille, J.; Betoule, M.; Melin, J.B.; Miville-Deschênes, M.A.; González-Nuevo, J.; Le Jeune, M.; Castex, G.; de Zotti, G.; Basak, S.; Ashdown, M.; Aumont, J.; Baccigalupi, C.; Banday, A.J.; Bernard, J.P.; Bouchet, F.R.; Clements, D.L.; da Silva, A.; Dickinson, C.; Dodu, F.; Dolag, K.; Elsner, F.; Fauvet, L.; Faÿ, G.; Giardino, G.; Leach, S.; Lesgourgues, J.; Liguori, M.; Macías-Pérez, J.F.; Massardi, M.; Matarrese, S.; Mazzotta, P.; Montier, L.; Mottet, S.; Paladini, R.; Partridge, B.; Piffaretti, R.; Prézeau, G.; Prunet, S.; Ricciardi, S.; Roman,

---

[1] https://github.com/mrbell/pyrmsynth

M.; Schaefer, B.; Toffolatti, L. The pre-launch Planck Sky Model: a model of sky emission at submillimetre to centimetre wavelengths. *A&A* **2013**, *553*, 96.

12. Tribble, P.C. Depolarization of extended radio sources by a foreground Faraday screen. *MNRAS* **1991**, *250*, 726–736.

13. Benjamin, R.A. What is the Reynolds Number of the Reynolds' Layer? *Interstellar Turbulence* **1999**, p. 49.

14. Vázquez-Semadeni, E. Hierarchical Structure in Nearly Pressureless Flows as a Consequence of Self-similar Statistics. *ApJ* **1994**, *423*, 681.

15. Passot, T.; Vázquez-Semadeni, E. Density probability distribution in one-dimensional polytropic gas dynamics. *Phys. Rev. E* **1998**, *58*, 4501.

16. Hill, A.S.; Benjamin, R.A.; Kowal, G.; Reynolds, R.J.; Haffner, L.M.; Lazarian, A. The Turbulent Warm Ionized Medium: Emission Measure Distribution and MHD Simulations. *ApJ* **2008**, *686*, 363–378.

17. Berkhuijsen, E.M.; Fletcher, A. Density probability distribution functions of diffuse gas in the Milky Way. *MNRAS* **2008**, *390*, L19–L23.

18. Sun, X.H.; Reich, W.; Waelkens, A.; Enßlin, T.A. Radio observational constraints on Galactic 3D-emission models. *A&A* **2008**, *477*, 573–592.

19. Jansson, R.; Farrar, G.R. A New Model of the Galactic Magnetic Field. *ApJ* **2012**, *757*, 14.

20. Heald, G.H. The Faraday rotation measure synthesis technique. *Cosmic Magnetic Fields: From Planets* **2009**, *259*, 591–602.

21. Schnitzeler, D.H.F.M.; Katgert, P.; de Bruyn, A.G. WSRT Faraday tomography of the Galactic ISM at $\lambda \sim$ 0.86 m. I. The GEMINI data set at (l, b) = (181°, 20°). *A&A* **2009**, *494*, 611–622.

22. Dickey, J.M.; Landecker, T.L.; Thomson, A.J.M.; Wolleben, M.; Sun, X.H.; Carretti, E.; Douglas, K.; Fletcher, A.; Gaensler, B.M.; Gray, A.D.; Haverkorn, M.; Hill, A.S.; Mao, S.A.; McClure- Griffiths, N.M. The Galactic Magneto-Ionic Medium Survey: Moments of the Faraday Spectra. *ApJ* **2018**, p. submitted.

23. Landecker, T.L.; Reich, W.; Reid, R.I.; Reich, P.; Wolleben, M.; Kothes, R.; Uyanıker, B.; Gray, A.D.; Del Rizzo, D.; Fürst, E.J.; Taylor, A.R.; Wielebinski, R. A Survey of the polarized emission from the Galactic plane at 1420 MHz with arcminute angular resolution. *A&A* **2010**, *520*, 80.